High-porosity thin membrane for high-efficiency capture of rare cells

Haoyue Luo, Feng Liang, Wei Wang, Xiaochen Huang, Zheng Mao, Li Wang, Jian Shi, Juan Peng, Yong Chen

High-porosity thin membrane for high-efficiency capture of rare cells

Haoyue Luo [a], Feng Liang [a], Wei Wang [a],
Xiaochen Huang [a], Zheng Mao [a], Li Wang [b], Jian Shi [b], Juan Peng [a*], and Yong Chen [a*]

[a] PASTEUR, Département de chimie, École normale supérieure, PSL University, Sorbonne Université, CNRS, 75005 Paris, France

[b] MesoBioTech, 231 Rue Saint-Honoré, 75001 Paris, France

e-mail: juan.wang@ens.psl.eu; yong.chen@ens.psl.eu

ABSTRACT

High efficiency capture of rare cells such as circulating tumor cells (CTCs) in the blood of cancer-patient is challenging for size-based separation methods, because of the heterogeneity of the cells, the presence of a huge number of background cells (red and white blood cells), and the overlap in size of the rare cells and some of the background cells. In this work, we developed a systematic study to evaluate the parametric dependence of rare cell capture efficiency by using model cells. High-porosity and thin membranes with a supporting honeycomb microframe are fabricated by using a two-level lithography technique. They are then integrated into a microfluidic device for real-time monitoring of flow-induced transmembrane pressure with a solution with or without cells. Our results show both experimentally and theoretically a great importance of the pore number of the membrane and the flow rate. When more than 80% of pores are clogged by large background cells, the rare cell capture efficiency decreases significantly. Otherwise, a lossless capture is theoretically achievable with a high-porosity and large-area membrane under optimal flow conditions.

Keywords: High porosity membrane, Microfluidics, Flow dynamics, Rare cell capture

1. Introduction

Detecting circulating tumor cells (CTCs) in the peripheric blood of cancer patients is possible but challenging for cancer prognosis and diagnosis [1]. Previous studies have shown that the presence of CTCs in patients' blood is a strong indication of cancer metastasis. However, it is hard to achieve a widely acceptable use policy, because of the complexity of the disease, the heterogeneity of CTCs, and the lack of prominent markers with respect to the huge number of background cells in blood (mostly white blood cells, WBCs). Indeed, CTCs are released by solid tumors with sophisticated tumor environments and they interact with immune and vessel cells as well as fibroblasts before and after entering the bloodstream so that they exhibit different phenotypes, survivability, and features [2,3]. For metastatic patients, one to a few hundred of CTCs can be found in a blood sample containing billions of Red Blood Cells (RBCs) and several tens of millions of WBCs, making them difficult to be captured and difficult to be identified. A variety of affinity-dependent or independent techniques have been proposed to overcome these difficulties but few of them have reached a maturation stage for clinical usage [4–6].

Typically, affinity-dependent capture relies on the interaction of epithelial cell adhesion molecules (EpCAM) of CTCs with anti-EpCAM antibodies immobilized on the surface of magnetic beads or patterned substrates [7–12]. Despite a large number of assays such as the Cellsearch platform, these techniques allow capture of $EpCAM^+$ CTCs only, since EpCAM makers were not expressed and expressed at a low level by CTCs experienced an epithelial-mesenchymal transition [13,14]. Combined use of several types of antibodies for multiple antigens was also tested, but it has to be generalized [15]. Alternatively, negative enrichment of CTCs by depleting all the CD45-specific leukocytes has been proposed, showing advantages of unbiased detection of CTCs but the possibility of exclusion of CTC-WBC clusters [16]. In contrast, affinity-independent methods are label-free and dependent only on the physical properties of CTCs such as size [17], deformability [18], density [19], and acoustic [20], and dielectrophoresis [21], which differ from blood cells. These techniques are often based on microfluidic chip technologies, which can be easily used for prototyping and accurate flow manipulation. However, many of them are limited to slow processing and a low CTCs recovery rate. More recently results have shown considerable interest in the combined use of both affinity-dependent and affinity-independent techniques [22,23] but yet the clinical criteria need to be met in terms of

detection accuracy, cost, and robustness.

Among different approaches, membrane-based filtration technology has received particular attention due to its simplicity, high throughput, low cost, and processing accuracy [17,18,24–27]. Basically, this technology applied to CTCs capture is cell size- and deformability-based, assuming that all cells of large sizes and relatively large Young's modulus, including CTCs can be captured by the membrane with a well-defined pore size. Once captured, these cells are subjected to downstream analyses so that a high efficiency capture of CTCs is primarily important. In the early period of development, track-etched membranes (TEM) of 8 μm pores were used [17] but less used later because of unevenly distributed or fused pores which limit the porosity of the membrane. Lithography-defined membranes (LDM) have been developed by photolithography and pattern-transfer techniques such as etching, lift-off, casting, and micro-molding. Different types of materials and pore structures have been studied to improve the CTCs detection sensibility [24–32], but only a few of them were devoted to studies of CTC-related flow dynamics [33–36]. In fact, the size of CTCs (12–25 μm) may partially overlap that of WBCs (5–20 μm) and similarly for both deformability and nuclear–cytoplasmic ratio of the cells [37]. Considering, however, the fact that only a fraction of WBCs may have comparable size and deformability to that of the targeting CTCs, it should be possible to tune the pore size and the flow condition precisely to capture both types of cells and allow passage of other cells. In such a case, the pore number of the membrane has to be significantly larger that of the background cells to avoid large increase of transmembrane pressure. In principle, this can be achieved by increasing the porosity and the size of the membrane as well as decreasing of the membrane thickness and the flow rate. To act without clear understanding of this principle, the potential of the membrane-based filtration technology in CTCs capture might be underestimated.

In this work, we developed a systematic and quantitative study to understand the flow dynamics dependence of rare cell capture by using a membrane-based microfluidic system and model cells. Tri-layer architecture and high-porosity membranes were produced by using photolithography and vacuum-assisted UV molding techniques which were then inserted into a microfluidic device with a solution with or without background cells and the addition of rare (tumor) cells. We first describe the fabrication techniques of tri-layer membrane, the microfluidic system used for parametric analyses, and cell processing protocols. Then, we present the results obtained with or without cells and compare

them with theory in terms of flow-induced and background cell-affected transmembrane pressure. Next, we show a significant decrease of the rare cell capture efficiency with the increase of the ratio between the cell number and the pore number of the membrane. We also show a good cell viability after capture with a high porosity membrane and a limited flowrate. Finally, we show the feasibility of using the present method for rare cell capture with blood samples.

2. Material and methods

2.1. Fabrication of High-Porosity Membrane

High-porosity membranes were prepared by one-step vacuum-assisted UV molding, in a similar way of the works [27,38]. A tri-level template was first fabricated by photolithography (SI Fig.S1). A chromium mask was patterned with a micro pattern generator (μPG 101, Heidelberg Instruments) for a hexagonal array of holes of 6, 7, and 8 μm diameter and 10 μm pitch size. Then, the mask was spin-coated with 2 and 7 μm thick SU-8 2002 (SU-8 2005) photoresist (MicroChem, France) and pre-baked on a 65 °C hotplate for 1 min and a 95 °C hotplate for 3 min. It was exposed to a UV light from the backside for 7 s and post-baked on a 65 °C hotplate for 1 min and a 95 °C hotplate for 4 min. Afterward, the resist was developed with SU-8 developer for 1 min and washed with isopropanol, resulting in the designed hexagonal array of holes (first layer). To enhance the mechanical stability of the membrane, a second layer of thick honeycomb microframe was added by spin coating a 40 μm thick SU-8 2015 photoresist (MicroChem, France) directly on the first layer. After being pre-baked on a 65 °C hotplate for 1 min and a 95 °C hotplate for 10 min, it was exposed to a UV light for 15 s through another chromium mask having a honeycomb lattice of 200 μm diameter and 25 μm linewidth, followed by a post-bake on a 65 °C hotplate for 1 min and a 95 °C hotplate for 10 min. Afterward, the resist was developed with SU-8 developer for 3 min and washed with isopropanol. Similarly, a ring of 180 μm thickness, 13 mm outer diameter, and 5, 7, or 9 mm diameter was added for handling. Secondly, after anti-sticking surface treatment, a mixture of PDMS pre-polymer and cross-linker (GE RTV 615) at a ratio of 5:1 was poured on. After curing at 75 °C for 2 h, the PDMS layer was peeled off, resulting in a negative-tone replica of the template. Finally, the PDMS layer was placed on a glass slide and degassed for 10 min in a desiccator. A solution of OrmoStamp (Micro Resist, Germany) was introduced to fill the cavity between the PDMS structure and the glass slide, followed by a UV exposure. After removal of the PDMS layer, the resulting membrane was peel-off from the glass slide.

2.2. Cell Preparation

Human ovarian cancer cells (SKOV3) and human liver cancer cells (HepG2) were used as model rare cells while Madin–Darby Canine Kidney (MDCK) cells were chosen as background cells due to their relatively smaller cell/nuclear sizes with respect to that of the targeting cells (SKOV3 and HepG2). MDCK cells were cultured in Minimum Essential Medium (MEM, Fisher Scientific, France) supplemented with 5 % fetal bovine serum (FBS, Sigma, France), 1 % penicillin-streptomycin (P/S, Fisher Scientific, France), and 1 % glutamine (Sigma, France). SKOV3 and HepG2 cells were cultured in RPMI-1640 medium developed by Roswell Park Memorial Institute (Fisher Scientific, France) and Dulbecco's modified Eagle's Medium containing 4.5 g/L glucose (DMEM, Fisher Scientific, France) respectively, supplemented with 10 % FBS and 1 % P/S at 37 °C in 5 % CO_2. Before cell capture, SKOV3 or HepG2 cells were firstly stained by 20 μg/ml Cell Tracker fluorescent probes Green BODIPY (Fisher Scientific, France), 10 μg/ml Hoechst 33342 (ThermoFisher, France) for 30 min and then washed with phosphate buffer saline (PBS, Sigma, France) 3 times. Finally, every sample included different numbers (0, 400 K, 800 K, 1200 K) of MDCK cells mixed with 1 K SKOV3 or HepG2 cells, which were prepared to pass through the filter, respectively. Fluorescence images were obtained with a Zeiss Observer Z1 fluorescence microscope. The tumor cells capture efficiency was calculated by the captured tumor cells number divided by the total tumor cells number.

2.3. Scanning Electron Microscopy Characterization

The membrane captured cells were fixed with 4 % paraformaldehyde (PFA, Sigma, France, diluted in PBS) for 15 min at room temperature. The samples were then rinsed with PBS three times. Next, the samples were dehydrated in 30 % ethanol solution (diluted in DI water) for 30 min and dehydrated by subsequent immersion in 50 %, 70 %, 80 %, 90 %, 95 % and 100 % ethanol solution (diluted in DI water), each for 10 min and dried with a vacuum pump for 10 min. Before scanning electron microscopy (SEM) observation, the samples were coated with a 2 nm thick gold layer by sputtering. A scanning electron microscope (TM3030, Hitachi, Japan) was used to observe samples with an accelerating voltage of 15 kV.

2.4. Cells Viability Assay

Cell viability was studied by live/dead assay. Briefly, 4 μM Calcein AM (Invitrogen, L3224) and 5 μM propidium iodide (Sigma-Aldrich, P4170) in 1mL PBS solution were added on the filter after

filtration for live and dead cell staining, respectively. After 30 min incubation at 37 °C and 5% CO_2, PBS was added into the device at 0.1 mL/min for 20 min. Finally, fluorescence images were also analyzed with a Zeiss Observer Z1 fluorescence microscope.

3. Results and discussion

3.1. Characteristics of High-Porosity Membrane

Shown in Fig. 1a-1c are sketch of the honeycomb frame supported membrane, SEM image of a honeycomb compartment with membrane, and SEM image of a membrane with captured cells. The geometry parameters of the membrane including pore size and pitch, honeycomb frame size and thickness, and membrane size and thickness can be defined by design. For comparison, membranes of 6, 7, and 8 μm pore size (D6, D7, and D8), 10 μm pitch, and 2 and 7 μm thickness (H2 and H7) with a honeycomb frame of 40 μm thickness, 25 μm line width, and 200 μm pitch were used. Unless specified, membranes of 9 mm inner diameter were used. To illustrate the high quality of the membrane structure but a non-vertical wall of the frame, SEM images of membrane series of D6H7, D7H7, D8H7, D6H2, D7H2, and D8H2 are shown in SI (Fig. S2). By using the above parameters, a membrane porosity of 0.45, 0.59, and 0.77 can be obtained for D6, D7, and D8 membrane, respectively. Ultimately, the fabrication with a membrane thickness less than 1 μm is achieved. Submicron features can be obtained on the master by backside exposure due to limited diffraction effect and then produced with a honeycomb frame of smaller openings. The wetting properties of the membrane were examined by measuring the contact angle of a DI water drop on the membrane. As expected, a contact angle of 54° and 22° was determined by photograph image analyses with the membrane before and after plasma surface treatment (SI Fig. S3).

We previously presented the fabrication of conical pore membranes by using a similar molding technique [27]. It works well for rare cell capture with an improved capture efficiency but is limited in porosity since the diameter of the large opening of the holes cannot be reduced for a membrane of large thickness which is requested to keep good mechanic stability of the membrane. The tri-level membrane architecture proposed in this work allows largely decreasing the membrane thickness so that a high porosity can be achieved without losing the mechanical stability of the membrane. The effective in-plane and out-of-plane Young's modulus of a hexagonal frame can be calculated

numerically [41]. Within the zeroth-order approximation, they should be $\frac{4}{\sqrt{3}}E_s(\frac{d}{l})^3$ and $\frac{2}{\sqrt{3}}E_s(\frac{d}{l})$, respectively, where E_s is Young's modulus of bulk material, and d and l are respectively the diameter and length of the cellular segment of the frame [42]. Thus, for a honeycomb frame of d = 40 μm and l = 100 μm, the in-plane and out-of-plane Young's modulus of the frame should be $0.15E_s$ and $0.46E_s$, respectively. Similarly, the stiffness of the thin layer of the membrane can be estimated by simply considering the high porosity membrane structure as a honeycomb of d = 2 μm and l = 5 μm. Thus, the in-plane and out-of-plane Young's modulus of the membrane area should be comparable to that of the frame. Furthermore, based on the von Karman plate theory, the deflection of the membrane in each of the honeycomb compartments can be estimated assuming that the membrane is totally clogged by cells [43,44]. In the limit of small deflection and small Poisson's ratio, a linear dependence relation can be approximated, $w = 3Pa^4/16Eh^3$, where w is the membrane deflection in the center of the compartment, P is the pressure, a is the compartment size, h is the thickness of the membrane [45]. Assuming a = 100 μm, h = 2 (7) μm, P = 1 kPa, and $E = 1G$Pa, a small deflection, w = 2.3 (0.05) μm, is expected. If the membrane of all compartment areas is clogged by cells, however, the deflection can be significantly larger due to much increased transmembrane pressure (see below).

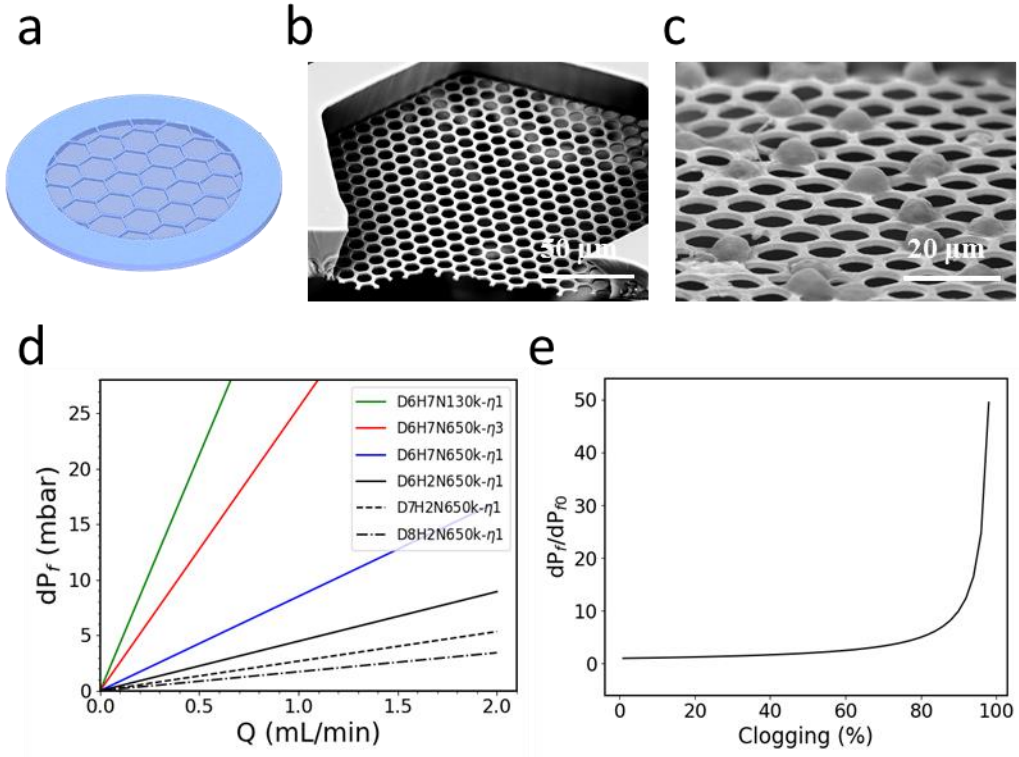

Fig. 1. High porosity thin membrane and flow-induced transmembrane pressure with or without cells. (a) Sketch of a high-porosity membrane with a supporting honeycomb frame. (b) SEM images of high-porosity membranes with 8 µm pore size and 2 µm thickness (D8H2). (c) Clogging of the membrane by large background cells. (d) Numerical results of flow-induced transmembrane pressure with different flow conditions (*D*: diameter, *H*: thickness, *N*: pore number, η: viscosity). (e) Numerical results of flow induced transmembrane pressure as a function of percentage of membrane clogging due to the presence of large number and large size background cells.

3.2. Numerical Calculation of Transmembrane Pressure

To optimize the experimental condition, the flow-induced transmembrane pressure (dP_f) was analyzed by using the following formula derived from Navier-Stocks equation [36,39,40]

$$dP_f = \frac{24\eta Q}{ND^3}\left(1 + \frac{16H}{3\pi D}\right) \quad (1)$$

where η is the viscosity of the solution, Q is the flow rate, *N* is the number of pores, D is the pore size in diameter, and *H* is the thickness of the membrane. Fig. 1d shows dP_f as a function of *Q*, calculated by using Eq.1 for six sets of geometry-viscosity parameters. Here, D6H7N650k notes a membrane of 6 µm pore size (D), 7 µm thickness (H), and 650 000 pore number (N), η1 notes a

solution of 1 cP viscosity (η), and so on. As expected, and for a given value of Q, dP_f increases with the membrane thickness but decreases rapidly with the pore size. In addition, dP_f is linearly proportional to η but inversely proportional to N. Since the escape probability (see below) and the damage of a capture cell increases with dP_f, it is a benefit for rare cell capture to limit the flow rate, to increase the pore number, and to decrease the membrane thickness and the viscosity of the solution. To maximize the capture efficiency, D should be smaller than the nuclei size of the rare cells. In practice, however, Q can be more easily adjusted to trade off the capture selectivity of a real sample.

Once a cell is captured by the membrane, it will be subjected to the flow induced transmembrane pressure which impacts to the cell behavior. Depending on the amount of pressure, the pore size and thickness and the viscosity of the solution, the cell can stay on the membrane or escape through the pore. Depending on the amount of pressure, the cell can also be alive or dead. By correlating the flow rate and the membrane properties to the cellular characteristics, it would be possible to optimize the flow conditions and to reach a maximum of rare cell capture efficiency. With the increase of the number of captured cells, the number of open pores decreases and accordingly the transmembrane pressure increases due to clogging. This can be calculated by considering the number of open pores before (N_0) and after (N) clogging

$$\frac{dP_f}{dP_{f0}} = \frac{N_0}{N} = \frac{1}{1-dN/N_0}, \qquad (2)$$

where dP_{f0} is the transmembrane pressure without clogging and dN/N_0 is the presentation of pore clogging. As can be seen, when the clogging level is higher than 85%, the transmembrane pressure increases rapidly (Fig. 1e). Since the rare cells are immerged among a huge number of background cells with variable sizes, they can be captured with a small portion but a considerable number of large size background cells. Therefore, it is important to increase the pore number in order to preserve a high capture efficiency of rare cells.

3.3. Microfluidic System for Rare Cells Capture

The fabricated membrane was reversibly integrated into a microfluidic device made of two plastic plates and a sample loading cylinder (Fig. 2a). The upper plate has two Luer connectors and an open access of 10 mm diameter with a screw mount structure for the sample loading cylinder. A thin layer of PDMS was added to the lower surface of the plate for sealing. The lower plate has embedded

channels with access holes and a 10 mm inner diameter semi-open chamber, sealed with a thin layer of PDMS. In addition, a thin layer of PDMS with a 14 mm diameter opening and two access holes was bound on the surface of the lower plate for positioning the membrane insert. After inserting the membrane, the two plates could be mechanically clamped with a mounting device and four hand screw nuts. To improve the uniformity of cell distribution over the membrane surface during filtration, a flow dispenser was fabricated by 3D printing and inserted in the sample loading cylinder.

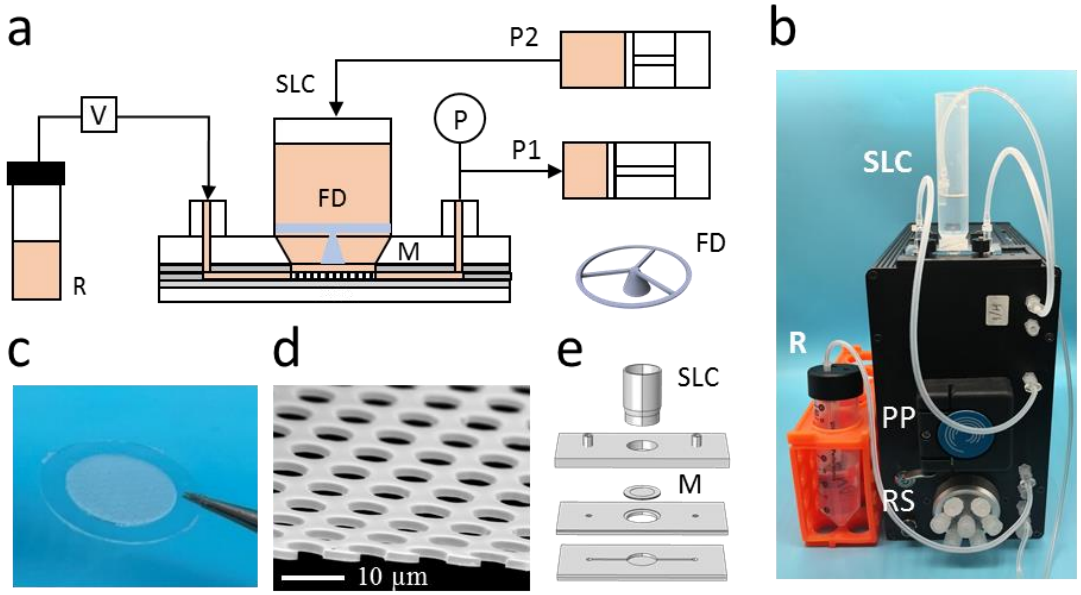

Fig. 2. Experiment setup. (a) Schematic diagram of the setup: P1, P2: Syringe pumps, P: Differential pressure gauge, V: Solenoid valve, R: Reservoir, SLC: Sample loading cylinder, and FD: Flow disperser, M: membrane. (b) Photograph of the setup with an additional peristatic pump (PP) and a rotational switch (RS). All other components are inside the box. (c, d) Photograph and SEM images of a D7H2 membrane. (d) Sketch of a microfluidic device with a filtration membrane and a sample loading cylinder.

A solution with or without cells was introduced into the container and pulled with a syringe pump through one of the embedded channels and integrated membrane at a constant flow rate (Fig. 2b). The pressure in the lower chamber was recorded with a differential pressure gauge of model MPX5010DP (RS Components, France). In addition, the inlet of the lower plate was connected to a reservoir, and

an electromagnetic valve was inserted in the pipeline to release, if necessary, the lower chamber pressure. As the recorded pressure is the sum of the hydraulic pressure and the transmembrane pressure, which depend respectively on the filling level of the cylinder and the flow rate, a second syringe pump was used to replenish the cylinder for the measurements with constant hydraulic pressure. All electronic components, including the two syringe pumps, the electromagnetic valve, and the differential pressure gauge were controlled with a PC and a Python script for automated processing.

3.4. Flow Dynamics of the System without Cell

Before investigating the performance of rare cell capture, the fabricated membranes were characterized with PBS solution without cells. After wetting the lower chamber and injecting 5 mL PBS into the sample loading cylinder, the solution was pulled with syringe pump P1 across the membrane at a constant flow rate. The pressure variation in the lower chamber was then recorded in real-time, knowing that the recorded pressure (dP) is the difference of the hydraulic pressure (dP_h) and the flow-induced transmembrane pressure (dP_f). Here, dP_h is a relative value in reference to the level of the pressure sensor and the flow resistance of the system except dP_f is neglected. Fig. 3a shows the pressure variation as a function of pulling time with a D7H7 membrane at a flow rate of 0.2, 0.5, 1, and 2 mL/min respectively. As can be seen, immediately after pulling the pressure dropped which depends critically on the flow rate. While it is difficult to determine the pressure drop with the two lowest flow rates (0.2 and 0.5 mL/min), the drastic pressure drop with the two higher flow rates (1 and 2 mL/min) can be measured. This can be understood by considering the flow induced transmembrane pressure, as described before). Once the syringe pump is started, a negative pressure is built underneath the membrane to drive the flow cross the membrane, together with the hydraulic pressure. Be using the following parameters, D = 7 µm and H = 7 µm, N = 650 K, and η = 1 cP, a dP_f of 5 and 10 mbar can be obtained with a flow rate of 1 and 2 mL/min, respectively, in good agreement with the experiment. A dP_f of 1.0 and 2.5 mbar is also predicted but not observed at a flow rate of 0.2 and 0.5 mL/min, respectively, due probably to the inertia of the system. After the initial pressure drop, dP decreased smoothly until another sudden change. This smooth period measured ~7 mbar is due to the change in dP_h. The shape of the slow decreasing as a function of time is determined by the geometry characteristics of the sample loading cylinder (the cylinder diameter decreases slowly in the upper part and then varies rapidly to fit the entrance of the chip, as depictured in Fig. 2a). The

drastic pressure drop in Fig. 3a was due to the empty of the solution and the turning point measured the lower chamber pressure just before empty. However, the pressure values recorded were only relative since they depended on the relative height of the chip with reference to the height of the pressure gauge. The time needed to pull out the solution which is proportional to Q for the same volume of sample loading can also be verified with the same curves.

Fig. 3b shows the influence of pore size on the flow dynamics of the system with a flow rate of 2 mL/min. Again, the flow rate induced pressure drop can be analyzed, which is critically dependent on the pore size, as predicted by Equation (1). Note also that the time needed to pull out the solution decreased slightly with the increase of pore size, due probably to the difference in the onset of a regular flow before reaching a stable flow rate. Similarly, the influence of membrane thickness can be analyzed, as shown in Fig. 3c. Now, the pressure change was recorded for two types of membranes with a flow rate of 1 and 2 mL/min. As expected, dP_f was sensitive to both membrane thickness and flow rate. The thicker the membrane, the larger the flow rate induced pressure drop and the time needed to pull out the solution is proportional to Q, in agreement with the prediction of Equation (1).

In order to more clearly show the change in dP_f, the sample loading cylinder was replenished during the solution pulling by using P2 so that dP_h was kept as constant. Fig. S4 shows a comparison of the recorded change of the system (dP) with or without replenishing, by using a D7H7 membrane and a flow rate of 0.5 mL/min. As expected, dP of the system with replenishment remained unchanged during pulling so that any pressure change will depend only on the change of other parameters. Similarly, the pressure change of the system with repeatedly solution renewing was tested each time the sample cylinder became empty (Fig. 3d). Interestingly, once the cylinder was filled, the initial dP can be recovered but the effective pumping speed of the first cycle was significantly smaller than the following ones and it became stable after 2 ~ 3 cycles, due probably to the improvement of wetting properties of the system.

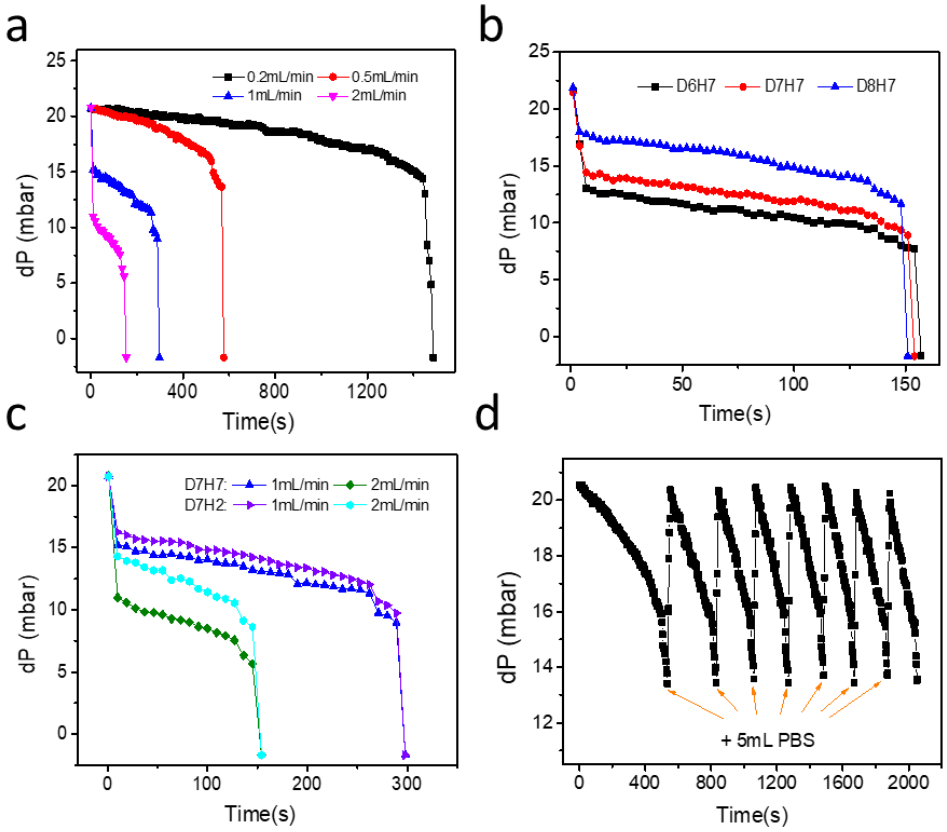

Fig. 3. Recorded pressure as a function of pulling time, with a D7H7 membrane and a solution of 5 mL PBS at 0.5 mL/min flow rate, unless specified. (a) Effect of flow rate (0.2, 0.5, 1, and 2 mL/min). (b) Effect of pore size (6, 7, and 8 μm) at a 2 mL/min flow rate. (c) Effect of membrane thicknesses (2 and 7 μm). (d) Effect of PBS refilling.

3.5. Flow Dynamics of the System with Cells

In the presence of cells, the flow dynamics of the system can be changed not only due to the change in viscosity but also due to the problem of clogging. In practice, CTCs are always immerged in blood with a huge number of background cells (WBCs), among them larger size and/or less deformable cells do exist. MDCK cells were chosen to simulate these cells due to their reasonable sizes and stiffnesses (Fig. S5). This, cell-containing PBS solutions with a MDCK cell number in the range of 150 K (150 000) to 1200 K (1 200 000). Fig. S6 shows SEM images of captured MDCK cells on D8H7, D8H2 and D7H7 membranes. Since the average nuclear size of MDCK cells (8 μm) is slightly larger than the pore size, some cells could be captured and some others can pass through the pores. As can be seen, the pore sizes of the membranes are slightly smaller than the cell sizes and most captured cells are above the pores but some are above the joint areas of the pores. A previous study has

shown the interest of minimizing the membrane thickness, because of the decrease in both requested pressure and cell deformation [46].

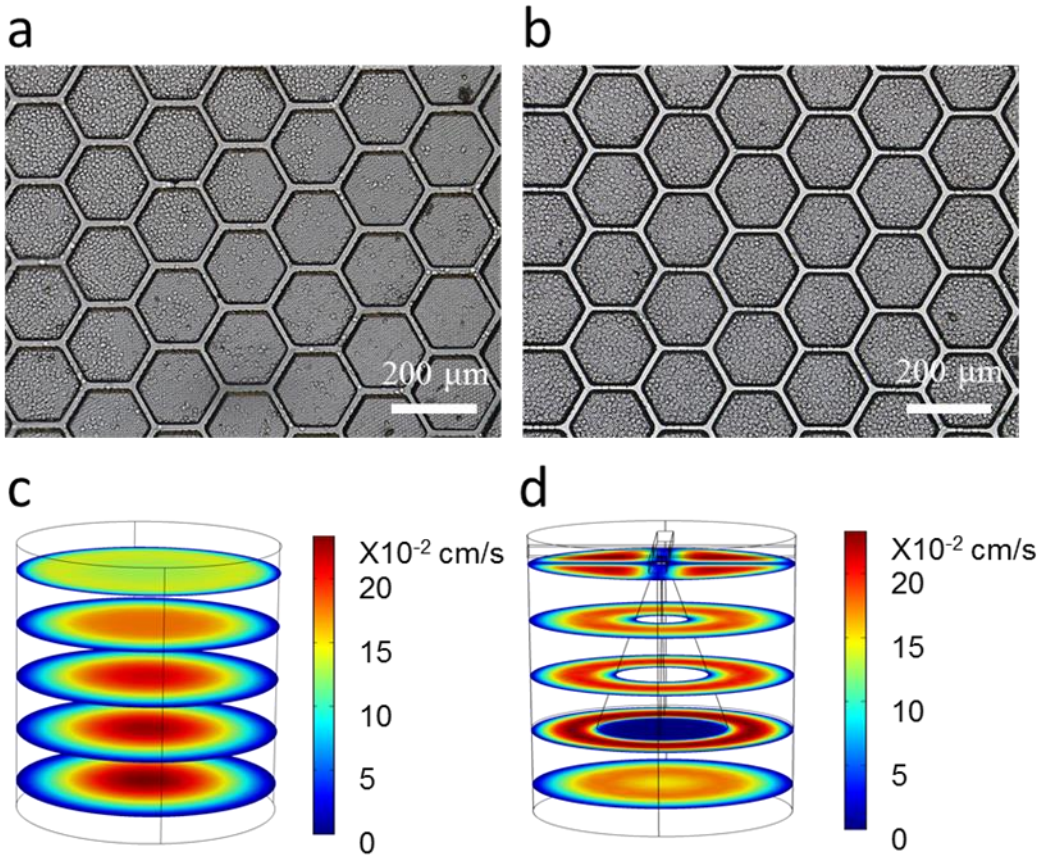

Fig. 4. Effect of flow disperser. (a, b) Bright-field images of D7H7 membrane close with captured MDCK cells without (a) or with (b) the help of a flow disperser. Both images were taken in the off-center area of the membrane. (c, d) Stimulation results of flow density above the membrane without (c) or with (d) a flow disperser. Cell number: 800 K; Flowrate: 0.2 mL/min.

In all the experiments with cells, the 3D printed flow disperser was inserted in the sample loading cylinder to uniformize the cell distribution on the membrane by pulling. In Fig. 4, bright-field images of MDCK cells obtained using a 9 mm inner diameter membrane and a sample loading cylinder with or without flow disperser, are compared, illustrating a much-improved uniformity of the cell density. Numerical results obtained with the same device configuration using COMSOL Multiphysics software (COMSOL France SAS, France) are also displayed, in agreement with experiments.

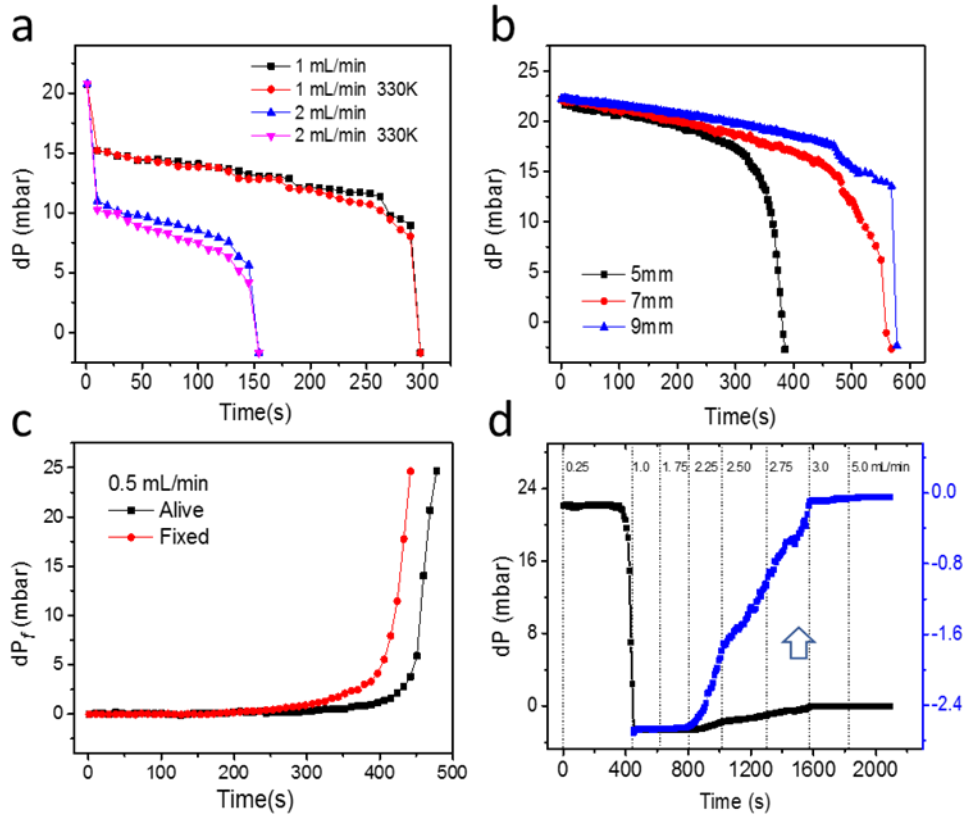

Fig. 5. Recorded pressure as a function of pulling time, with a D7H7 membrane and a cell containing 5 mL PBS solution at a flow rate of 0.5 mL/min unless specified. (a) Effect of flow rate with 330 K MDCK cells. (b) Effect of membrane size with 330 K MDCK (5, 7, and 9 mm inner diameter and 6 μm pore size). (c) Effect of cell fixation with 800 K MDCK cells and a D6H7 membrane. (d) Effect of flow rate with 800 K MDCK cells (flow rate of 0.25 to 1.0, 1.75, 2.25, 2.75, 3.0, and 5 mL/min).

As discussed above, dP_f is membrane geometry and flow rate dependent which can easily reach a pressure drop of several hundred and several thousand Pascals, which covers a wide spectrum of cellular stiffnesses of mammalian [37]. We firstly examined the flow dynamics with background cells (MDCK) and then the efficiency of rare cell capture by including larger cells (SKOV3 and HepG2) (Fig. S5). Fig. 5a shows a comparison of flow dynamics between PBS and a PBS solution containing 330 K MDCK cells. Here, the cell number is about half of the pore number of the membrane to guarantee a still high permeability of the membrane. As expected, comparable changes in dP_f and dP_h were found that with or without cells but the effect of clogging could be clearly observed at a flow rate of 2 mL/min. According to Equation (1), the decrease of open pores (N) due to clogging may

introduce an increase in dP_f, in addition to a decrease of dP_h during pulling.

We further examined the effect of cell capture induced clogging on the flow dynamics of the system by using membranes of the same pore geometry (D6H7) but the different inner diameters of a membrane (5, 7, and 9 mm) which consisted of 201 K, 393 K, and 650 K pores, respectively. Under the same flow conditions with a 5 mL PBS solution containing 330 K MDCK cells and a flow rate of 0.5 mL/min, the three membranes resulted in significant differences in flow dynamics (Fig. 5b). In the case of a 9 mm diameter membrane, the cell number is much smaller than that of pore number (650 K). dP decreased with time quasi-linearly to about 470 s and then decreased irregularly before a drastic following down, due to the change in dP_f and dP_h, as discussed above. In the case of a 7 mm diameter membrane, the cell number is close to the pore number (393 K) so that most of pores could be clogged by cells after 450 s and dP decreased more rapidly. However, the membrane was still somehow permeable and the flow rate could be nearly maintained.

In contrast, in the case of a 5 mm diameter membrane the cell number is significantly larger that the pore number (201 K) so that most pores of the membrane could be blockaded after 250 s, resulting a rapid decrease of the lower chamber pressure. At about 380 s, the membrane became non-permeable and the lower chamber might be vacuumed. Under such a large pressure difference, the captured cells may be escaped if the pore is sufficiently large. Indeed, we did observe the effect of complete membrane clogging with membranes of 6 μm pore size because of the comparable sizes of the cell nuclei and the pore. Here, a membrane of 6 μm pores was chosen to evidence the clogging effect caused by cell capture and the importance of pore numbers. We can then conclude that to avoid the loss of captured cells, the pore number must be significantly larger than the number of cells which may block the pores. As shown in Fig. 1d, dP_f decreases with the decrease in membrane thickness. It is therefore important to produce high-porosity, large area, and thin membranes for more efficient rare cell capture.

By using 800 K MDCK cells with or without fixation, a similar effect could be observed with a membrane of 9 mm inner diameter and a flow rate of 0.5 mL/min with replenishment (Fig. 5c). Now, dP_h is constant and dP_f can be plotted to show more clearly the effect of cell capture induced clogging. Without fixation, dP_f was unchanged during the first 300 s, then increased smoothly to about 450 s. Afterward, it drastically increased and reached a large value of dP_f at about 480 s due

to cell capture induced membrane clogging. With cells after fixation, similar behavior was observed but the membrane clogging occurred earlier due to more efficient clogging with fixed cells. Theoretically, this can be predicted by using Equation (1) (Fig. 1e), in agreement with the experiment.

The flow dynamics with cells were also studied by using the same type of membrane and a similar flow condition except for the sequential addition of 150 K MDCK cells in the sample loading cylinder (Fig. S7). As can be observed, after adding cells for three times, dP still increased, meaning that the membrane was still permeable but the effect of cell captured induced clogging could be noticed by the decrease of peak pressure value due to an increased dP_f or a decreased number of open pores. Adding 150 K more cells, the number of cells (600 K) became comparable to the pore number of the membrane so that the effect of clogging became dominant.

Finally, the effect of cell loss with large flow rates was studied by using a membrane of D7H7 and 800 K MDCK cells. Fig. 5d shows the variation of dP after a sequential increase of pulling flow rate from 0.25 to 1.0, 1.75, 2.25, 3.0, and 5.0 mL/min. Clearly, with a flow rate of 0.25 mL/min, the membrane was rapidly clogged. Increasing of the flow rate to 1.0 and 1.75 had no effect to the cell escape. After switching to a flow rate of 2.25, dP_f became large enough to cause a continuous loss of captured cells. A further increase of the flow rate to 2.5 and 2.75 mL/min had a similar effect. Once switched to a flow rate of 3.0 mL/min, dP_f remained unchanged, indicating a complete loss of the membrane-captured cells. Numerical calculation predicted that with a bare membrane of 650 K pores without cells, a flow rate of 2.25 will generate a dP_f of about 11.25 mbar. With 80 % of cell pore clogging, dP_f is about 56.25 mbar which is largely sufficient to pull the captured cells away.

3.6. Capture Efficiency of Rare Cells

To investigate the influence of background cells on the capture of rare cells, 1K SKOV3 or HepG2 tumor cells were spiked in 5 mL PBS solution containing 0, 400 K, 800 K, or 1200 K MDCK cells. SKOV3 and HepG2 cells were chosen as model rare cells because of their relatively large cell size and large nuclei. For comparison, D7H7 and D7H2 membranes and a flow rate of 0.2 mL/min were used to minimize the transmembrane pressure and show the clogging effect and the clogging induced cell loss.

As expected, the capture efficiency of rare cells of both types decreased with the increase of the number of background cells (Fig. 6a and c). When the number of background cells was significantly

smaller than the pore number, all rare cells could be captured. When the number of background cells (800 K) was larger than the pore number, the capture efficiency decreased to 99.4 % (SKOV3) and 98.9 % (HepG2), respectively. When the number of background cells increased to 1200 K which is almost twice the pore number, the capture efficiency of both rare cells decreased drastically, showing 85.2 % and 81.9 % efficiency respectively. The decrease in the rare cell capture efficiency can be understood in terms of the retention of background cells and the increase of dP_f. Fig. 6b and d display the pressure change (dP) under different filtration conditions. Interestingly, small differences in time can be observed. It took about 1350 s or 1365 s to pump out the solution, depending on whether the cell number is smaller or larger than the pore number. As discussed before, the variation in dP before the sudden drop is due to the change in both dP_h and dP_f. While the change in dP_h was the same for all the measurements, dP_f increased with the decrease in number of open pores, indicating more clearly the clogging effect with the increase of MDCK cell numbers. However, this effect was less significant when a D7H2 membrane was used since MDCK cells could more easily pass through the membrane. Compared with the D6H7 membrane with which the membrane could be completely clogged by the MDCK cells (Fig. 5b), both D7H7 and D7H2 membranes remained permeable for MDCK cells due to their comparable nuclear sizes with respect to the pore size. However, the clogging effect with a large number of MDCK cells may cause a significant loss of the target cells (SKOV3 and HepG2), corresponding to a remarkable decrease in rare cell capture efficiency. To avoid such a decrease, the solution is simply increasing the pore number of the membrane. In order to demonstrate the effect of the ratio of background cells to rare cells on the capture efficiency, 10 SKOV3 cells were also spiked in 5 mL PBS solution containing 400 K, 800 K, or 1200 K MDCK cells. As expected, the capture efficiency of SKOV3 cells decreased with the increase of the number of background cells (Fig. S8). And the capture efficiencies of SKOV3 cells in different number of background cells (400 K, 800 K and 1200 K) are 100 %, 96.7 % and 86.7 %, respectively, which are similar to the capture efficiencies of 1 K SKOV3 cells in background cells (400 K, 800 K and 1200 K). However, the ratio of background cells to rare cells has a 100-fold increase, which is close to the ratio in real blood sample. The results illustrated that the ratio of background cells to rare cells have no remarkable effect on the capture efficiency, which is mainly affected by the clogging effect with a large number of background cells.

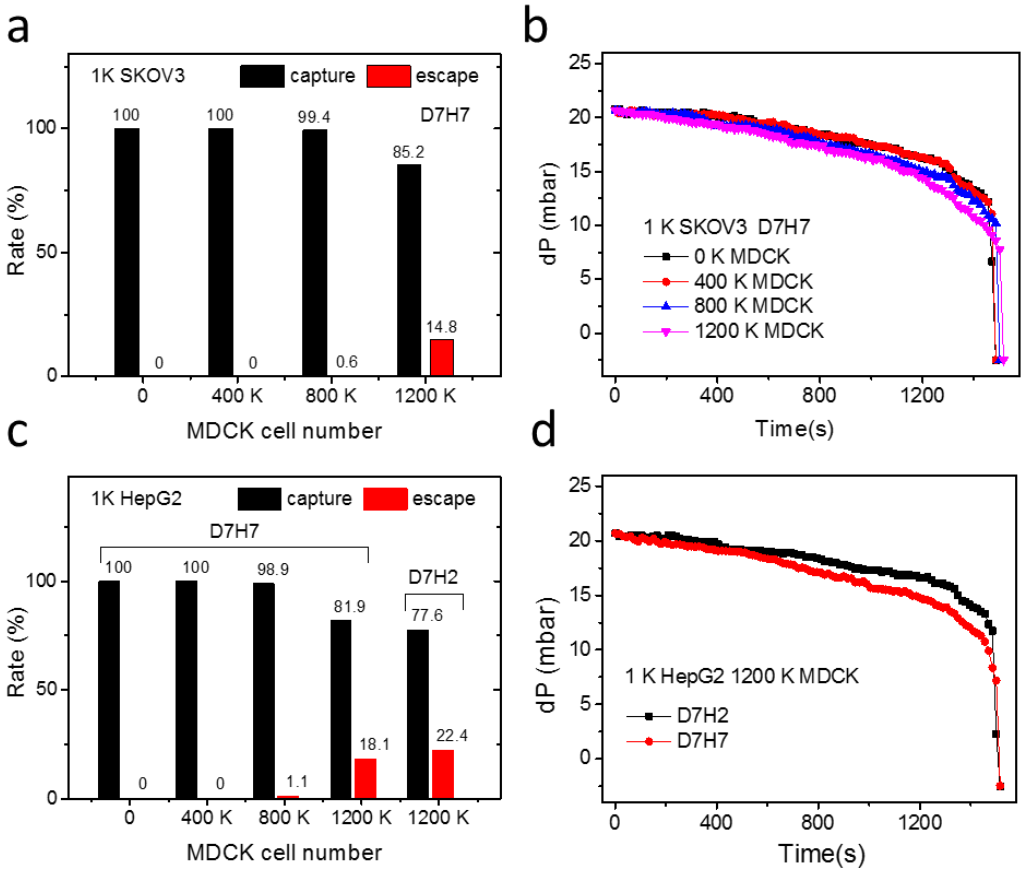

Fig. 6. Capture and escape rate of 1K SKOV3 or HepG2 cells spiked in a PBS solution with background cells of different cell numbers (0, 400, 800, and 1200 K MDCK), using D7H7 and D7H2 membrane of 9 mm inner diameter (650 K pores).

WBCs are composed of granulocytes (neutrophils, eosinophils, and basophils) and non-granulocytes (lymphocytes and monocytes). While granulocytes are the most numerous of the white cells and are approximately 12–15 μm in diameter, they have a multilobed nucleus with Young's modulus of about 150 Pa. Lymphocytes have variable sizes with relative low Young's modulus, meaning that both granulocytes and lymphocytes can be easily deformed to pass through the membrane of 7 μm pores at a typical flow rate of 0.5 mL/min. Finally, monocytes measure 12-20 μm [5], 9.7–10.5 μm [37], or 8-13 μm [47] in diameter with a relative larger Young's modulus. Statistically, most of WBCs are lymphocytes and granulocytes and only about 2 – 8 % of WBCs are monocytes. So far, it is not clear how these cells migrate through a thin membrane with well-defined pore size and pore density at a given flowrate. Reasonably, at least a few percent of WBCs have larger sizes than targeting rare cells so that without cell deformation and migration, the membrane can be easily clogged. Previous

studies have shown that CTCs can have a wide range of size distribution (7-24 μm) but a relatively large Young's modulus (500 – 2000 Pa) than WBCs, suggesting that it is hard to achieve a high selectivity or high purity of CTCs by using size- and deformation-based capture due to the overlap of two types of cells. Assuming a 50 % pore clogging with a D7H7 membrane, a transmembrane pressure of dP_f > 5 mbar (flow rate of 0.6 mL/min) should be effective to wash away small and medium WBCs keeping both rare cells and larger and stiffer WBCs on the membrane. Ultimately, a membrane of diameter of 20 mm and porosity of 0.92, pore pitch size of 8 μm will be sufficient to be only half blocked by large and stiff WBCs in 5 mL blood.

3.7. Cell Viability Assessment

In general, the viability of captured cells is sensitive to the flow dynamics. The smaller the dP_f, the better the cell viability. dP_f depends on the relative number of background cells with the reference of the pore number of the membrane, the viability of captured cells was evaluated by spiking 600 K and 1200 K MDCK cells in PBS solution and Calcein AM and propidium iodide staining based live/dead assays. As shown in Fig. S9, about 97.0 % of captured cells were alive in the case of 600 K cell spiking whereas the cell viability decreased to 87.9 % in the case of 1200 K spiking due to largely increased dP_f. As discussed above, for a given number of background cells and pore size, increasing the pore number of a membrane leads to a decrease of dP_f so that the larger the pore size, the better the cell viability. Similarly, decreasing the membrane thickness leads to a decrease in dP_f so also an increase in the viability of captured cells.

3.8. Test with Blood Samples

Blood samples with spiked SKOV3 cells were used to test the potential relevance of the method for CTC capture. For each sample, 4 ml blood was diluted in PBS at a volume ratio of 1:1 without red blood cells. The filtration experiments were performed with D7H2 and D7H7 membrane at a flow rate of 0.3 ml/min. After filtration and immunostaining, fluorescence images of cells captured on the filters were recorded (green for CK positive, red for CD45 positive, blue for nuclei of all cells). Fig. S10 the results of filtration. As can be seen, the number of captured blood cells on D7H7 is significantly larger than that on the D7H2 membrane (Fig. S10a and b), suggesting an easy escape of captured cells from the thinner membrane of the same pore size and the same pore density. This can be understood by considering the migration behavior of leukocytes despite differences in transmembrane pressure

[48,49]. Our preliminary results of flowcytometry showed that the most captured WBCs are lymphocytes. More systematic analyses need to be carried out in order to clarify the subtypes of these cells. Statistically, less than 30% of D7H2 membrane pores were clogged, in consistent with the measured small transmembrane pressure. However, about 80% of D7H7 pores were clogged, which followed into a critical regime of transmembrane pressure variation. Experimentally, we recorded an unstable increase of transmembrane pressure during the course of filtration. An optimal membrane thickness has to be worked out for clinical applications. Fig. S10c and d show zoomed fluorescence images with and without a CK positive cell. Clearly, CD45 positive cells are located in the pore area and a clear correlation between DAPI and CK positive/CD45 negative or CD45 positive/CK negative can be found, which allowed us to attribute the CK positive and CD45 negative cells to the tumor cell. A more systematic investigation will be conducted with for a more relevant assessment of this method.

3.9. Limitation and Potential of the Method

We would like to mention that although the fabrication presented in this work is straightforward, other techniques such as nanoimprinting will be needed for mass production and large-scale applications of the high-porosity membranes. This work is limited to using model cells but similar studies can be performed with the blood of healthy donors with spiking cells or cancer patients. In order to adjust more efficiently the parameters of membrane geometry and flow rate, it is necessary to obtain, by using the same technique, more detailed information on size and deformability profiling of WBCs. Further improvements including surface functionalization of the membrane, multichannel processing, automatic staining, high throughput imaging, and digital PCR analyses are envisageable based on the present work.

In reference to the previous discussions and assessments [4,50], several issues on the utility of filtration techniques can now be addressed, including low sensibility, limited heterogeneity, clogging, long process, cell viability, standardization, etc. By using the new type of membrane developed, the pore size is defined according to the (cell) nuclei sizes, and the flow rate is adjusted with real-time monitoring to have a limited transmembrane pressure to prevent the loss and damage of captured cells. Nevertheless, with a large number of background cells, the purity cannot be high, but this might be not an issue if the captured CTC can be identified by staining with appropriate markers [51] and/or single cell analysis [3]. With the further improvement of the detection method [52–55], it might be possible

to largely reduce the probability of false negative. Reasonably with a membrane of 2 times larger (18 mm in diameter), the pore number increases by a factor of 4 so that the actual flow rate (0.5 mL/min) can be increased to 2 mL/min. This flow rate is sufficient for fast processing and eventually in vivo assays. By considering patient-specific tumor characteristics and the constant need for more efficient anti-cancer drugs, many interesting topics on CTCs have been discussed [56], including tumor microenvironment [2], epithelial-mesenchymal transition [57], cancer stem cells, in vitro expansion and xenograft models [58], multicellular clusters [59], drug resistance [60], early cancer screening [61], and immunotherapy [62]. With an improved understanding and a new technology perspective, these issues can certainly be addressed more readily.

4. Conclusions

We systematically investigated the flow dynamics of a membrane-based filtration system for high efficiency capture of rare cells in the presence of a large number of background cells. High-porosity membranes were produced using photolithography and one-step vacuum-assisted UV molding techniques. Prior to the cell capture studies, the membrane properties and the flow dynamics of the system were analyzed under different flow conditions. By adding a large number of model background cells that simulate the large-size WBCs, we found that the flow-induced transmembrane pressure was highly dependent on the ratio of the cell number to the pore number of the membrane. Our results showed both theoretically and experimentally that if 80 % of the pores were clogged by cells, the transmembrane pressure increased drastically. We also found that if the number of the background cells was significantly less than the pore number of the membrane, a high efficiency capture of the rare cells could be reached and otherwise, the capture efficiency decreased rapidly. Thus, we propose the following design principles: i) the pore size should be smaller than that of the CTC nuclei, ii) the pore number of the membrane should be significantly larger than that of larger WBCs, iii) the thickness of the membrane and the flow rate should both be justified to achieve an optimize capture efficacy.

Ethical statement

Blood samples have been collected from donors that were fully informed regarding the purposes of the study and consent was obtained. All the experiments performed in this work involving human samples were approved with Guangzhou Anfang Biotechnology Co., Ltd.

Credit author statement

H.L. drafted manuscript, performed the device preparation and data collection, J.P., F.L., W.W., X.H. and Z.M. aided in methodology, L.W. and J.S. helped in mask and microfluidic device making, Y.C. planed and supervised the work. All authors discussed the results and commented on the manuscript.

Declaration of Competing Interest

The authors declare that they have no known competing financial interests or personal relationships that could have appeared to influence the work reported in this paper.

Acknowledgments

H.L. is grateful to the China Scholarship Council for grant of his PhD studies. We are grateful to R. Liu, J.Y. Zhou, and Dr C. Han (Guangzhou Anfang Biotechnology Co., Ltd.) for assistance and helpful discussions.

Appendix A. Supplementary data

Supplementary data associated with this article can be found, in the online version, at https://doi.org/10.1016/j.snb.xxxx.xxxxxx.

References

[1] L. Descamps, D. Le Roy, A.-L. Deman, Microfluidic-Based Technologies for CTC Isolation: A Review of 10 Years of Intense Efforts towards Liquid Biopsy, IJMS. 23 (2022) 1981. https://doi.org/10.3390/ijms23041981.

[2] K.E. De Visser, J.A. Joyce, The evolving tumor microenvironment: From cancer initiation to metastatic outgrowth, Cancer Cell. 41 (2023) 374–403. https://doi.org/10.1016/j.ccell.2023.02.016.

[3] P. Radfar, H. Aboulkheyr Es, R. Salomon, A. Kulasinghe, N. Ramalingam, E. Sarafraz-Yazdi, J.P. Thiery, M.E. Warkiani, Single-cell analysis of circulating tumour cells: enabling technologies and clinical applications, Trends in Biotechnology. 40 (2022) 1041–1060. https://doi.org/10.1016/j.tibtech.2022.02.004.

[4] V. Akpe, T.H. Kim, C.L. Brown, I.E. Cock, Circulating tumour cells: a broad perspective, J. R. Soc. Interface. 17 (2020) 20200065. https://doi.org/10.1098/rsif.2020.0065.

[5] J.F. Edd, A. Mishra, K.C. Smith, R. Kapur, S. Maheswaran, D.A. Haber, M. Toner, Isolation of circulating tumor cells, IScience. 25 (2022) 104696. https://doi.org/10.1016/j.isci.2022.104696.

[6] M. Vidlarova, A. Rehulkova, P. Stejskal, A. Prokopova, H. Slavik, M. Hajduch, J. Srovnal, Recent Advances in Methods for Circulating Tumor Cell Detection, IJMS. 24 (2023) 3902. https://doi.org/10.3390/ijms24043902.

[7] S. Nagrath, L.V. Sequist, S. Maheswaran, D.W. Bell, D. Irimia, L. Ulkus, M.R. Smith, E.L. Kwak, S. Digumarthy, A. Muzikansky, P. Ryan, U.J. Balis, R.G. Tompkins, D.A. Haber, M. Toner, Isolation of rare circulating tumour cells in cancer patients by microchip technology, Nature. 450 (2007) 1235–1239. https://doi.org/10.1038/nature06385.

[8] S. Riethdorf, L. O'Flaherty, C. Hille, K. Pantel, Clinical applications of the CellSearch platform in cancer patients, Advanced Drug Delivery Reviews. 125 (2018) 102–121. https://doi.org/10.1016/j.addr.2018.01.011.

[9] W. Sheng, O.O. Ogunwobi, T. Chen, J. Zhang, T.J. George, C. Liu, Z.H. Fan, Capture, release and culture of circulating tumor cells from pancreatic cancer patients using an enhanced mixing chip, Lab Chip. 14 (2014) 89–98. https://doi.org/10.1039/C3LC51017D.

[10] Q. Wu, L. Zhu, X. Wei, M. Zhang, C. Zhang, Z. You, S. Zhang, Y. Song, D. Liu, C. Yang, Detection of circulating tumor cells using antibody-functionalized microchips to monitor tumorigenesis in a mouse model of metastatic breast cancer, Sensors and Actuators B: Chemical. 379 (2023) 133274. https://doi.org/10.1016/j.snb.2022.133274.

[11] S. Wang, H. Wang, J. Jiao, K.-J. Chen, G. Owens, K. Kamei, J. Sun, D. Sherman, C. Behrenbruch, H. Wu, H.-R. Tseng, Three-Dimensional Nanostructured Substrates toward Efficient Capture of Circulating Tumor Cells, Angew. Chem. Int. Ed. 48 (2009) 8970–8973. https://doi.org/10.1002/anie.200901668.

[12] V.S. Goudar, P.-H. Yeh, S.-Y. Wu, C.-H. Chu, L.-S. Lu, C.-H. Yang, T.-J. Chiou, F.-G. Tseng, Live circulating tumour cells selection on digitized self-assembled cell array (Digi-saca) chip by in-parallel/in-situ image analysis, cell capture, and cultivation, Sensors and Actuators B: Chemical. 316 (2020) 128002. https://doi.org/10.1016/j.snb.2020.128002.

[13] F. Farace, C. Massard, N. Vimond, F. Drusch, N. Jacques, F. Billiot, A. Laplanche, A. Chauchereau, L. Lacroix, D. Planchard, S. Le Moulec, F. André, K. Fizazi, J.C. Soria, P. Vielh, A direct comparison of CellSearch and ISET for circulating tumour-cell detection in patients with metastatic carcinomas, Br J Cancer. 105 (2011) 847–853. https://doi.org/10.1038/bjc.2011.294.

[14] M. Yu, A. Bardia, B.S. Wittner, S.L. Stott, M.E. Smas, D.T. Ting, S.J. Isakoff, J.C. Ciciliano, M.N. Wells, A.M. Shah, K.F. Concannon, M.C. Donaldson, L.V. Sequist, E. Brachtel, D. Sgroi, J. Baselga, S. Ramaswamy, M. Toner, D.A. Haber, S. Maheswaran, Circulating Breast Tumor Cells Exhibit Dynamic Changes in Epithelial and Mesenchymal Composition, Science. 339 (2013) 580–584. https://doi.org/10.1126/science.1228522.

[15] G. Deng, M. Herrler, D. Burgess, E. Manna, D. Krag, J.F. Burke, Enrichment with anti-cytokeratin alone or combined with anti-EpCAM antibodies significantly increases the sensitivity for circulating tumor cell detection in metastatic breast cancer patients, Breast Cancer Res. 10 (2008) R69. https://doi.org/10.1186/bcr2131.

[16] Z. Liu, A. Fusi, E. Klopocki, A. Schmittel, I. Tinhofer, A. Nonnenmacher, U. Keilholz, Negative enrichment by immunomagnetic nanobeads for unbiased characterization of circulating tumor cells from peripheral blood of cancer patients, J Transl Med. 9 (2011) 70. https://doi.org/10.1186/1479-5876-9-70.

[17] G. Vona, A. Sabile, M. Louha, V. Sitruk, S. Romana, K. Schütze, F. Capron, D. Franco, M. Pazzagli, M. Vekemans, B. Lacour, C. Bréchot, P. Paterlini-Bréchot, Isolation by Size of Epithelial Tumor Cells, The American Journal of Pathology. 156 (2000) 57–63. https://doi.org/10.1016/S0002-9440(10)64706-2.

[18] E.S. Park, C. Jin, Q. Guo, R.R. Ang, S.P. Duffy, K. Matthews, A. Azad, H. Abdi, T. Todenhöfer, J. Bazov, K.N. Chi, P.C. Black, H. Ma, Continuous Flow Deformability-Based Separation of Circulating Tumor Cells Using Microfluidic Ratchets, Small. 12 (2016) 1909–1919. https://doi.org/10.1002/smll.201503639.

[19] H.J. Woo, S.-H. Kim, H.J. Kang, S.-H. Lee, S.J. Lee, J.M. Kim, O. Gurel, S.Y. Kim, H.R. Roh, J. Lee, Y. Park, H.Y. Shin, Y.-I. Shin, S.M. Lee, S.Y. Oh, Y.Z. Kim, J.-I. Chae, S. Lee, M.H. Hong, B.C. Cho, E.S. Lee, K. Pantel, H.R. Kim, M.S. Kim, Continuous centrifugal microfluidics (CCM) isolates heterogeneous circulating tumor cells via full automation, Theranostics. 12 (2022) 3676–3689. https://doi.org/10.7150/thno.72511.

[20] P. Li, Z. Mao, Z. Peng, L. Zhou, Y. Chen, P.-H. Huang, C.I. Truica, J.J. Drabick, W.S. El-Deiry, M. Dao, S. Suresh, T.J. Huang, Acoustic separation of circulating tumor cells, Proc. Natl. Acad. Sci. U.S.A. 112 (2015) 4970–4975. https://doi.org/10.1073/pnas.1504484112.

[21] S.-B. Huang, M.-H. Wu, Y.-H. Lin, C.-H. Hsieh, C.-L. Yang, H.-C. Lin, C.-P. Tseng, G.-B. Lee, High-purity and label-free isolation of circulating tumor cells (CTCs) in a microfluidic platform by using optically-induced-dielectrophoretic (ODEP) force, Lab Chip. 13 (2013) 1371. https://doi.org/10.1039/c3lc41256c.

[22] Z. Eslami-S, L.E. Cortés-Hernández, C. Alix-Panabières, Epithelial Cell Adhesion Molecule: An Anchor to Isolate Clinically Relevant Circulating Tumor Cells, Cells. 9 (2020) 1836. https://doi.org/10.3390/cells9081836.

[23] N.M. Karabacak, P.S. Spuhler, F. Fachin, E.J. Lim, V. Pai, E. Ozkumur, J.M. Martel, N. Kojic, K. Smith, P. Chen, J. Yang, H. Hwang, B. Morgan, J. Trautwein, T.A. Barber, S.L. Stott, S. Maheswaran, R. Kapur, D.A. Haber, M. Toner, Microfluidic, marker-free isolation of circulating tumor cells from blood samples, Nat Protoc. 9 (2014) 694–710. https://doi.org/10.1038/nprot.2014.044.

[24] M. Hosokawa, T. Hayata, Y. Fukuda, A. Arakaki, T. Yoshino, T. Tanaka, T. Matsunaga, Size-Selective Microcavity Array for Rapid and Efficient Detection of Circulating Tumor Cells, Anal. Chem. 82 (2010) 6629–6635. https://doi.org/10.1021/ac101222x.

[25] X. Ren, B.M. Foster, P. Ghassemi, J.S. Strobl, B.A. Kerr, M. Agah, Entrapment of Prostate Cancer Circulating Tumor Cells with a Sequential Size-Based Microfluidic Chip, Anal. Chem. 90 (2018) 7526–7534. https://doi.org/10.1021/acs.analchem.8b01134.
[26] A.F. Sarioglu, N. Aceto, N. Kojic, M.C. Donaldson, M. Zeinali, B. Hamza, A. Engstrom, H. Zhu, T.K. Sundaresan, D.T. Miyamoto, X. Luo, A. Bardia, B.S. Wittner, S. Ramaswamy, T. Shioda, D.T. Ting, S.L. Stott, R. Kapur, S. Maheswaran, D.A. Haber, M. Toner, A microfluidic device for label-free, physical capture of circulating tumor cell clusters, Nat Methods. 12 (2015) 685–691. https://doi.org/10.1038/nmeth.3404.
[27] Y. Tang, J. Shi, S. Li, L. Wang, Y.E. Cayre, Y. Chen, Microfluidic device with integrated microfilter of conical-shaped holes for high efficiency and high purity capture of circulating tumor cells, Sci Rep. 4 (2014) 6052. https://doi.org/10.1038/srep06052.
[28] S. Khetani, M. Mohammadi, A.S. Nezhad, Filter-based isolation, enrichment, and characterization of circulating tumor cells, Biotechnology and Bioengineering. 115 (2018) 2504–2529. https://doi.org/10.1002/bit.26787.
[29] L.S. Lim, M. Hu, M.C. Huang, W.C. Cheong, A.T.L. Gan, X.L. Looi, S.M. Leong, E.S.-C. Koay, M.-H. Li, Microsieve lab-chip device for rapid enumeration and fluorescence in situ hybridization of circulating tumor cells, Lab Chip. 12 (2012) 4388. https://doi.org/10.1039/c2lc20750h.
[30] Y. Liu, H. Xu, W. Dai, H. Li, W. Wang, 2.5-Dimensional Parylene C micropore array with a large area and a high porosity for high-throughput particle and cell separation, Microsyst Nanoeng. 4 (2018) 13. https://doi.org/10.1038/s41378-018-0011-8.
[31] J.A. Hernández-Castro, K. Li, J. Daoud, D. Juncker, T. Veres, Two-level submicron high porosity membranes (2LHPM) for the capture and release of white blood cells (WBCs), Lab on a Chip, 2019, 19(4): 589-597. https://doi.org/10.1039/C8LC01256C.
[32] H.J. Woo, S.H. Kim, H.G. Kang, T. Kim, S. Kim, J.M. Kim, J.Y. Kim, S.J. Lee, Y.Z. Kim, S.Y. Oh, J.H. Lim, H.M. Ryu, M.S. Kim, Lossless Immunocytochemistry Based on Large-Scale Porous Hydrogel Pellicle for Accurate Rare Cell Analysis, ACS Applied Materials & Interfaces, 2023, 15(12): 15059-15070. https://doi.org/10.1021/acsami.2c18321.
[33] D.L. Adams, P. Zhu, O.V. Makarova, S.S. Martin, M. Charpentier, S. Chumsri, S. Li, P. Amstutz, C.-M. Tang, The systematic study of circulating tumor cell isolation using lithographic microfilters, RSC Adv. 4 (2014) 4334–4342. https://doi.org/10.1039/C3RA46839A.
[34] M. Aghaamoo, Z. Zhang, X. Chen, J. Xu, Deformability-based circulating tumor cell separation with conical-shaped microfilters: Concept, optimization, and design criteria, Biomicrofluidics. 9 (2015) 034106. https://doi.org/10.1063/1.4922081.
[35] F.A.W. Coumans, G. Van Dalum, M. Beck, L.W.M.M. Terstappen, Filter Characteristics Influencing Circulating Tumor Cell Enrichment from Whole Blood, PLoS ONE. 8 (2013) e61770. https://doi.org/10.1371/journal.pone.0061770.
[36] F.A.W. Coumans, G. Van Dalum, M. Beck, L.W.M.M. Terstappen, Filtration Parameters Influencing Circulating Tumor Cell Enrichment from Whole Blood, PLoS ONE. 8 (2013) e61774. https://doi.org/10.1371/journal.pone.0061774.
[37] S.-J. Hao, Y. Wan, Y.-Q. Xia, X. Zou, S.-Y. Zheng, Size-based separation methods of circulating tumor cells, Advanced Drug Delivery Reviews. 125 (2018) 3–20. https://doi.org/10.1016/j.addr.2018.01.002.
[38] J.A. Hernández-Castro, K. Li, A. Meunier, D. Juncker, T. Veres, Fabrication of large-area polymer microfilter membranes and their application for particle and cell enrichment, Lab Chip. 17 (2017)

1960–1969. https://doi.org/10.1039/C6LC01525E.
[39] K.H. Jensen, A.X.C.N. Valente, H.A. Stone, Flow rate through microfilters: Influence of the pore size distribution, hydrodynamic interactions, wall slip, and inertia, Physics of Fluids. 26 (2014) 052004. https://doi.org/10.1063/1.4876937.
[40] R. Holdich, S. Kosvintsev, I. Cumming, S. Zhdanov, Pore design and engineering for filters and membranes, Phil. Trans. R. Soc. A. 364 (2006) 161–174. https://doi.org/10.1098/rsta.2005.1690.
[41] L.J. Gibson, M.F. Ashby, Cellular Solids: Structure and Properties, 2nd ed., Cambridge University Press, 1997. https://doi.org/10.1017/CBO9781139878326.
[42] Y. He, E. Rofaani, X. Huang, B. Huang, F. Liang, L. Wang, J. Shi, J. Peng, Y. Chen, Generation of Alveolar Epithelium Using Reconstituted Basement Membrane and hiPSC‐Derived Organoids, Adv Healthcare Materials. 11 (2022) 2101972. https://doi.org/10.1002/adhm.202101972.
[43] M. Radiom, Y. He, J. Peng‐Wang, A. Baeza‐Squiban, J. Berret, Y. Chen, Alveolar mimics with periodic strain and its effect on the cell layer formation, Biotechnology and Bioengineering. 117 (2020) 2827–2841. https://doi.org/10.1002/bit.27458.
[44] E. Rofaani, Y. He, J. Peng, Y. Chen, Epithelial folding of alveolar cells derived from human induced pluripotent stem cells on artificial basement membrane, Acta Biomaterialia. 163 (2023) 170–181. https://doi.org/10.1016/j.actbio.2022.03.022.
[45] Y. Zhang, Large deflection of clamped circular plate and accuracy of its approximate analytical solutions, Sci. China Phys. Mech. Astron. 59 (2016) 624602. https://doi.org/10.1007/s11433-015-5751-y.
[46] Y. Quan, Z. Zhu, D. Tang, S. Zhu, C. Wang, K. Chen, Z. Ni, An ultra-thin silicon nitride membrane for label-free CTCs isolation from whole blood with low WBC residue, Separation and Purification Technology. 296 (2022) 121349. https://doi.org/10.1016/j.seppur.2022.121349.
[47] K. Menck, D. Behme, M. Pantke, N. Reiling, C. Binder, T. Pukrop, F. Klemm, Isolation of Human Monocytes by Double Gradient Centrifugation and Their Differentiation to Macrophages in Teflon-coated Cell Culture Bags, JoVE. (2014) 51554. https://doi.org/10.3791/51554.
[48] J.S. Kuo, Y. Zhao, P.G. Schiro, L.Ng, D.S. Lim, J.P. Shelby, D.T. Chiu. Deformability considerations in filtration of biological cells. Lab Chip. 10 (2010) 837-42. doi: 10.1039/b922301k.
[49] D. Onoshima**,** T. Hase, N. Kihara, D. Kuboyama, H. Tanaka, N. Ozawa, H. Yukawa, M. Sato, K. Ishikawa, Y. Hasegawa, M. Ishii, M. Hori, and Y. Baba, Leukocyte Depletion and Size-Based Enrichment of Circulating Tumor Cells Using a Pressure-Sensing Microfiltration Device, ACS Meas. Sci. 3 (2023), 113–119, https://doi.org/10.1021/acsmeasuresciau.2c00057.
[50] S. Singh, P.S. Podder, M. Russo, C. Henry, S. Cinti, Tailored point-of-care biosensors for liquid biopsy in the field of oncology, Lab Chip. 23 (2023) 44–61. https://doi.org/10.1039/D2LC00666A.
[51] D. Lin, L. Shen, M. Luo, K. Zhang, J. Li, Q. Yang, F. Zhu, D. Zhou, S. Zheng, Y. Chen, J. Zhou, Circulating tumor cells: biology and clinical significance, Sig Transduct Target Ther. 6 (2021) 404. https://doi.org/10.1038/s41392-021-00817-8.
[52] S. Sharma, R. Zhuang, M. Long, M. Pavlovic, Y. Kang, A. Ilyas, W. Asghar, Circulating tumor cell isolation, culture, and downstream molecular analysis, Biotechnology Advances. 36 (2018) 1063–1078. https://doi.org/10.1016/j.biotechadv.2018.03.007.
[53] Z. Shen, A. Wu, X. Chen, Current detection technologies for circulating tumor cells, Chem. Soc. Rev. 46 (2017) 2038–2056. https://doi.org/10.1039/C6CS00803H.

[54] A. Strati, A. Markou, E. Kyriakopoulou, E. Lianidou, Detection and Molecular Characterization of Circulating Tumour Cells: Challenges for the Clinical Setting, Cancers. 15 (2023) 2185. https://doi.org/10.3390/cancers15072185.

[55] L. Ruiyi, P. Tinling, C. Hongxia, S. Jinsong, L. Zaijun, Electrochemical detection of cancer cells in human blood using folic acid and glutamic acid-functionalized graphene quantum dot-palladium@gold as redox probe with excellent electrocatalytic activity and target recognition, Sensors and Actuators B: Chemical. 309 (2020) 127709. https://doi.org/10.1016/j.snb.2020.127709.

[56] D. Hanahan, Hallmarks of Cancer: New Dimensions, Cancer Discovery. 12 (2022) 31–46. https://doi.org/10.1158/2159-8290.CD-21-1059.

[57] J. Yang, P. Antin, G. Berx, C. Blanpain, T. Brabletz, M. Bronner, K. Campbell, A. Cano, J. Casanova, G. Christofori, S. Dedhar, R. Derynck, H.L. Ford, J. Fuxe, A. García de Herreros, G.J. Goodall, A.-K. Hadjantonakis, R.Y.J. Huang, C. Kalcheim, R. Kalluri, Y. Kang, Y. Khew-Goodall, H. Levine, J. Liu, G.D. Longmore, S.A. Mani, J. Massagué, R. Mayor, D. McClay, K.E. Mostov, D.F. Newgreen, M.A. Nieto, A. Puisieux, R. Runyan, P. Savagner, B. Stanger, M.P. Stemmler, Y. Takahashi, M. Takeichi, E. Theveneau, J.P. Thiery, E.W. Thompson, R.A. Weinberg, E.D. Williams, J. Xing, B.P. Zhou, G. Sheng, On behalf of the EMT International Association (TEMTIA), Guidelines and definitions for research on epithelial–mesenchymal transition, Nat Rev Mol Cell Biol. 21 (2020) 341–352. https://doi.org/10.1038/s41580-020-0237-9.

[58] Z. Eslami-S, L.E. Cortés-Hernández, F. Thomas, K. Pantel, C. Alix-Panabières, Functional analysis of circulating tumour cells: the KEY to understand the biology of the metastatic cascade, Br J Cancer. 127 (2022) 800–810. https://doi.org/10.1038/s41416-022-01819-1.

[59] E. Schuster, R. Taftaf, C. Reduzzi, M.K. Albert, I. Romero-Calvo, H. Liu, Better together: circulating tumor cell clustering in metastatic cancer, Trends in Cancer. 7 (2021) 1020–1032. https://doi.org/10.1016/j.trecan.2021.07.001.

[60] N. Vasan, J. Baselga, D.M. Hyman, A view on drug resistance in cancer, Nature. 575 (2019) 299–309. https://doi.org/10.1038/s41586-019-1730-1.

[61] D. Crosby, S. Bhatia, K.M. Brindle, L.M. Coussens, C. Dive, M. Emberton, S. Esener, R.C. Fitzgerald, S.S. Gambhir, P. Kuhn, T.R. Rebbeck, S. Balasubramanian, Early detection of cancer, Science. 375 (2022) eaay9040. https://doi.org/10.1126/science.aay9040.

[62] A. Rzhevskiy, A. Kapitannikova, P. Malinina, A. Volovetsky, H. Aboulkheyr Es, A. Kulasinghe, J.P. Thiery, A. Maslennikova, A.V. Zvyagin, M. Ebrahimi Warkiani, Emerging role of circulating tumor cells in immunotherapy, Theranostics. 11 (2021) 8057–8075. https://doi.org/10.7150/thno.59677.